Tuijin Jishu/Journal of Propulsion Technology
ISSN: 1001-4055
Vol. 46 No. 2 (2025)

# Performance Assessment of a Newly Designed Cardiovascular Stent Using WE43 and Zn-0.8Li-0.4Mg Biocompatible Alloys

**Md. Shams Tabraiz Alam[1], Shabana Urooj[2,*], Abdul Quaiyum Ansari[1]**

[1] Dept of Electrical Engineering, Jamia Millia Islamia, New Delhi, India

[2] Dept of Electrical Engineering, College of Engineering, Princess Nourah Bint Abdulrahman University, P.O. Box 84428, Riyadh 11671, Saudi Arabia

*Corresponding Author, Email ID: SMUrooj@pnu.edu.sa

**Abstract:**

Cardiovascular stents play a vital role in treating narrowed arteries, where structural efficiency and biocompatibility are critical for long-term success. Material selection and design geometry significantly influence the mechanical performance of stents. Existing stent designs often suffer from limitations such as high foreshortening, dogboning, and recoiling, which can compromise deployment accuracy and arterial conformity. To address these limitations, this study explores both geometric optimization and novel biocompatible materials to enhance mechanical behaviour during stent expansion. The primary aim is to evaluate and compare a newly proposed stent design with an existing model using WE43 material, and further assess performance improvements using a Zn-0.8Li-0.4Mg alloy. The proposed WE43 stent design shows a remarkable reduction in foreshortening, dropping from 5.74% in the baseline paper considered for this study to just 0.79% at 0.05 mm thickness, significantly enhancing deployment precision. Dogboning remains well-controlled, increasing only slightly from –0.038% to 1.65% at the same thickness, while still staying within acceptable clinical limits. Recoiling improves notably at higher thicknesses dropping from 17.1% to 8.03% at 0.3 mm indicating improved radial stability. Compared to Zn–0.8Li–0.4Mg, WE43 exhibits more consistent foreshortening (~0.79–1.2%) and lower dogboning, confirming its superior mechanical performance for reliable cardiovascular deployment. The study establishes the significance of geometry and material synergy in stent design. Zn-0.8Li-0.4Mg emerges as a promising candidate for next-generation cardiovascular stents with improved deployment characteristics.

**Keywords: Geometry Optimization, Foreshortening, Dogboning, Recoiling, Biocompatible Materials, Finite Element Analysis**

## Introduction

Cardiovascular diseases, particularly coronary artery disease, are a leading cause of mortality globally, accounting for approximately 17.9 million deaths annually [1]. Percutaneous coronary intervention (PCI) with stent implantation has revolutionized the treatment of occluded or narrowed arteries caused by atherosclerosis, restoring blood flow and improving patient outcomes [2]. Stents, small mesh-like tubular structures, mechanically support the vessel wall, prevent elastic recoil, and maintain luminal patency [3]. However, challenges such as in-stent restenosis, stent thrombosis, and long-term biocompatibility issues continue to drive innovation in stent materials and design [4]. This research investigates the optimization of cardiovascular stent geometry using a novel Zn-0.8Li-0.4Mg alloy, aiming to achieve a synergistic balance of mechanical performance, controlled degradation, and vascular compatibility to address these challenges.

The evolution of stent materials began with bare-metal stents (BMS) in the late 1980s, primarily made from stainless steel due to its high mechanical strength and corrosion resistance [5]. While effective in preventing acute vessel closure, stainless steel stents were associated with high rates of restenosis caused by neointimal hyperplasia [6]. To address this, cobalt-chromium (Co-Cr) and platinum-chromium (Pt-Cr) alloys were introduced in the early

2000s, offering thinner struts, improved flexibility, and enhanced radiopacity while maintaining radial strength [7]. Despite these advancements, permanent metallic stents posed risks of chronic inflammation, late stent thrombosis, and impaired vessel remodelling, prompting the development of drug-eluting stents (DES) [8]. DES, coated with antiproliferative drugs such as sirolimus or paclitaxel, significantly reduced restenosis rates by inhibiting smooth muscle cell proliferation [9].

The advent of drug-eluting stents (DES) in the early 2000s revolutionized stent technology by incorporating antiproliferative coatings, such as sirolimus or paclitaxel, to inhibit smooth muscle cell proliferation and significantly reduce restenosis rates to below 10% in many cases [10]. Despite their efficacy, DES introduced new challenges, including delayed endothelialization, which necessitated extended dual antiplatelet therapy (DAPT) and increased the risk of late and very late stent thrombosis [11]. These limitations prompted the development of bioresorbable stents (BRS), designed to provide temporary mechanical support during vessel healing and then degrade, allowing the vessel to resume its natural biomechanical function [12]. Early BRS utilized polymers, such as poly-L-lactic acid (PLLA), exemplified by the Absorb Bioresorbable Vascular Scaffold (BVS) [13]. While PLLA-based stents offered predictable degradation profiles, their thicker struts (often exceeding 150 μm) and lower radial strength compared to metallic stents led to higher rates of scaffold thrombosis, particularly in complex or calcified lesions [14].

Metallic bioresorbable stents, particularly those based on magnesium (Mg), were developed to address the mechanical limitations of polymeric BRS [15]. Magnesium alloys provided superior radial strength and thinner strut profiles but degraded too rapidly, often within weeks, releasing hydrogen gas that disrupted local tissue healing and caused inflammation [16]. Conversely, iron (Fe)-based stents exhibited excessively slow degradation, often taking years, rendering them impractical for clinical applications requiring temporary scaffolding [17]. These challenges highlighted the need for biodegradable materials with degradation rates aligned with the vascular healing timeline, typically 6–12 months [18].

Zinc (Zn)-based alloys have recently emerged as a promising alternative, offering degradation rates that closely match the vascular healing process [19]. Pure zinc, however, lacks the mechanical strength and corrosion control necessary for stent applications, often exhibiting brittle behavior and uneven degradation [20]. Alloying zinc with elements such as lithium (Li) and magnesium (Mg) enhances its mechanical properties, including tensile strength and ductility, while improving corrosion behavior and biocompatibility [21]. The Zn-0.8Li-0.4Mg alloy, incorporating 0.8% lithium and 0.4% magnesium, represents a significant advancement in biodegradable stent materials [22]. This alloy minimizes hydrogen evolution compared to magnesium-based stents, offers a degradation profile more suitable than iron-based alternatives, and supports endothelial cell proliferation, reducing the risk of adverse tissue responses [23]. Its mechanical properties, including a yield strength comparable to traditional metallic stents, make it a viable candidate for cardiovascular applications [24].

Parallel to material advancements, stent geometry plays a critical role in determining clinical performance, influencing mechanical behavior, vessel interaction, and hemodynamic outcomes [25]. Stent geometry encompasses parameters such as strut thickness, width, cross-sectional shape, and the configuration of interconnecting links, all of which affect flexibility, radial strength, and fatigue resistance [26]. Early stent designs, such as simple sinusoidal or zigzag patterns, provided adequate support but often struggled in tortuous or calcified arteries, leading to uneven stress distribution, vessel wall injury, and suboptimal deployment [27]. Modern computational tools, including finite element analysis (FEA), computational fluid dynamics (CFD), and topology optimization, have transformed stent design by enabling the creation of complex geometries tailored to specific clinical needs [28]. For example, open-cell and hybrid patterns improve vessel conformability, while thinner struts (below 100 μm) enhance flexibility and reduce thrombogenicity, though they require precise optimization to maintain sufficient radial force to prevent vessel recoil and streamlined strut shapes, rounded edges, and optimized link configurations can minimize flow disruption, enhance endothelialization, and reduce the risk of complications [29,30].

Stent geometry also profoundly impacts hemodynamic performance, as strut profiles and patterns influence blood flow dynamics [31]. Poorly designed geometries can cause flow disturbances, such as low shear stress zones, that

promote thrombus formation or neointimal hyperplasia [32]. For bioresorbable stents like those using Zn-0.8Li-0.4Mg, geometry must be carefully designed to account for the material's degradation dynamics, ensuring structural integrity throughout the resorption process [33].

The clinical implications of stent geometry optimization are profound, particularly for bioresorbable stents. Optimized designs can reduce mechanical stress on the vessel wall, minimize endothelial injury, and enhance healing by promoting uniform degradation. For the Zn-0.8Li-0.4Mg alloy, geometric tailoring is essential to leverage its unique properties, such as controlled corrosion and biocompatibility, to achieve optimal performance in complex coronary anatomies [34]. By addressing both material and geometric challenges, this approach aims to overcome the limitations of current stents, including restenosis, thrombosis, and incomplete vessel healing.

This study focuses on optimizing cardiovascular stent geometry using the Zn-0.8Li-0.4Mg alloy, integrating advanced computational modeling with experimental validation to achieve superior mechanical performance, controlled degradation, and biocompatibility. By refining strut patterns, thicknesses, and link configurations, the research seeks to enhance vessel conformability, minimize complications such as restenosis and thrombosis, and support vascular healing. The integration of a novel biodegradable alloy with cutting-edge geometric design addresses the multifaceted demands of modern cardiovascular interventions, offering a pathway toward safer, more effective stents. This work contributes to the ongoing evolution of bioresorbable stent technology, aligning material innovation, geometric precision, and clinical performance to improve patient outcomes.

## 2. METHODOLOGY

### 2.1 Stent Geometry and Design

The investigation employed a systematic geometric design approach based on the ZigWave stent architecture, incorporating interconnected zigzag structures to achieve optimal mechanical performance characteristics. The design methodology followed a structured four-phase development process to ensure geometric consistency and manufacturing feasibility across all thickness variations.

The initial design phase involved creating a fundamental 2D wave-like pattern featuring a single repeating unit with interconnected zigzag structures, as illustrated in Figure 1(a). This foundational pattern established the basic geometric relationships between strut elements and connector regions that define the overall mechanical behavior. The wave-like configuration was specifically engineered to provide uniform stress distribution during radial expansion while maintaining adequate flexibility for navigational requirements. The zigzag interconnection geometry was optimized to minimize stress concentration factors at junction points, thereby enhancing structural durability under cyclic loading conditions.

The second developmental phase transformed the planar pattern through geometric manipulation, flexing the 2D structure through 180° rotation to establish a semi-cylindrical configuration, as demonstrated in Figure 1(b). This intermediate geometric state represented a critical transition from planar to three-dimensional architecture, requiring careful consideration of curvature-induced stress modifications and geometric constraint effects. The semi-cylindrical formation maintained the fundamental zigzag relationships while introducing the radial geometry essential for cardiovascular applications.

The third phase involved complete cylindrical stent model creation through mirroring operations, generating the full ZigWave structure with clearly differentiated alternating segments, as shown in Figure 1(c). The mirroring technique ensured perfect geometric symmetry throughout the cylindrical architecture while maintaining the designed stress distribution characteristics. The alternating segment visualization facilitated quality control verification during the design process, enabling identification of potential geometric discontinuities or asymmetric features that could compromise mechanical performance.

The final design phase produced the complete stent geometry exhibiting a continuous ZigWave cell pattern throughout the entire cylindrical structure, as presented in Figure 1(d). This final configuration incorporated all design requirements while maintaining manufacturing feasibility for the specified thickness variations. The

continuous cell pattern ensured uniform mechanical behavior along the entire stent length, eliminating potential weak points or performance variations that could affect clinical deployment success.

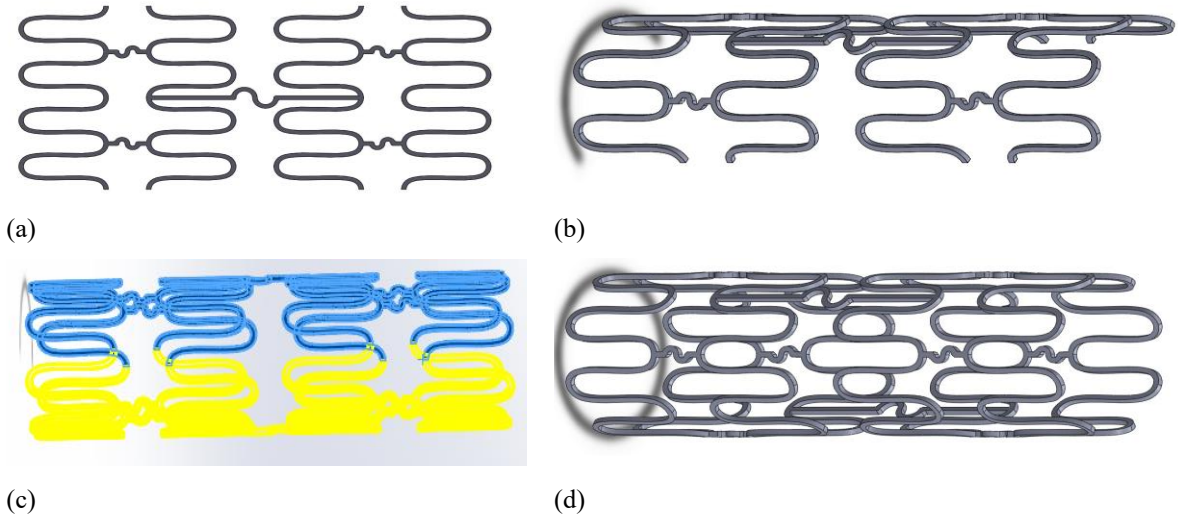


Figure 1: Design process of the ZigWave Stent: (a) 2D wave-like pattern displaying a single repeating unit with interconnected zigzag structures, (b) 2D pattern flexed 180° to form a semi-cylindrical shape, (c) complete cylindrical stent model created by mirroring, illustrating the full ZigWave structure with alternating blue and yellow segments, (d) final stent geometry showing the complete cylindrical form with a continuous ZigWave cell pattern.

The strut width parameter was maintained at a constant value of 0.1 mm throughout all design iterations, effectively eliminating width-induced variables and isolating the influence of thickness variations on mechanical performance. Six distinct stent configurations were systematically developed, incorporating thickness values of 0.05 mm, 0.1 mm, 0.15 mm, 0.20 mm, 0.25 mm, and 0.30 mm to comprehensively evaluate thickness-dependent behavioral characteristics. The geometric design criteria were established considering clinical deployment requirements specific to coronary artery interventions, emphasizing the critical balance between mechanical support capability and vessel wall compliance preservation.

Figure 2 illustrates the geometric variations resulting from thickness modifications in the ZigWave stent architecture. Figure 2(a) presents the cardiovascular stent with improved serpentine geometry configured at 0.3 mm thickness, demonstrating robust strut dimensions and enhanced structural features visible in the rectangular zoomed region. The substantial thickness provides pronounced three-dimensional characteristics essential for superior radial support capacity. Figure 2(b) shows the identical serpentine architecture at 0.05 mm thickness, revealing significantly reduced strut dimensions while preserving the fundamental geometric relationships. The rectangular zoomed view highlights the refined structural geometry at minimum thickness, emphasizing the precision required for ultra-thin configurations. This comparative visualization effectively demonstrates how thickness variations influence overall geometric complexity and mechanical behavior while maintaining consistent serpentine pattern architecture throughout the design spectrum.

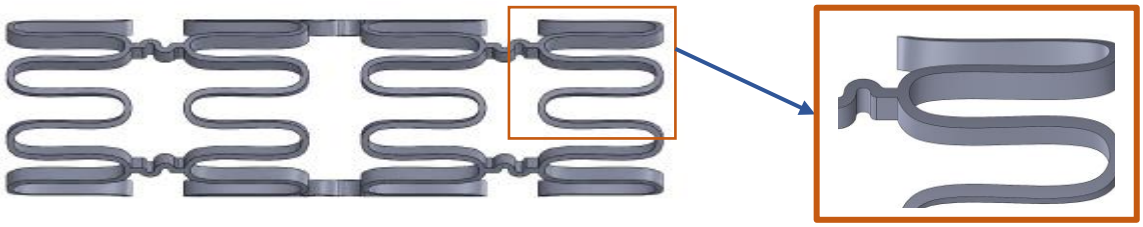

**Figure 2: Shows the Next-Generation Zigzag Cardiovascular Stent with Improved Link Geometry, designed with a thickness of 0.3 mm.** Zoomed View

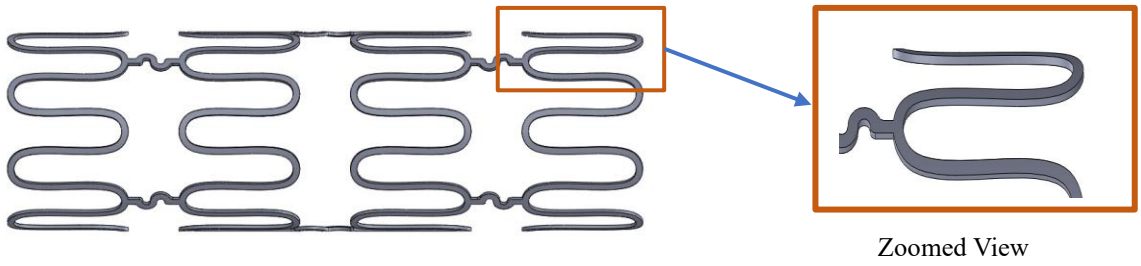


**Figure 2: Shows the Next-Generation Zigzag Cardiovascular Stent designed with a thickness of 0.05 mm.**

### 2.2 Material Properties

Two distinct materials were investigated in this study to evaluate the performance characteristics of biodegradable stent materials:

#### 2.2.1 Material Selection and Properties

In this study, WE43 magnesium alloy was adopted for modeling purposes, with its material properties sourced from the experimental data provided in reference [35], owing to its proven biocompatibility and biodegradability in cardiovascular stent applications. The zinc-based alloy Zn–0.8Li–0.4Mg was examined in this study due to its favorable mechanical characteristics and regulated degradation rate, positioning it as a strong candidate for future biodegradable stent applications [36]. Both materials were modeled as isotropic and assigned with their respective mechanical properties in the simulation environment.

. **Table 1: Material property of Stent**

| Property | WE43 Alloy | Zn–0.8Li–0.4Mg Alloy | **Units** |
|---|---|---|---|
| Young's Modulus | 44.2 | 100.5 | GPa |
| Yield Strength | 162 | 358.5 | MPa |
| Poisson's Ratio | 0.35 | 0.30 | -- |
| Density | 1.84 | 6.7 | g/cm³ |

To simulate the expansion process realistically, the balloon used for deployment was modeled as a hyperelastic material using the Mooney-Rivlin formulation. The material constants C10, C01, and D1 were selected from literature to reflect the nonlinear elastic behavior of commonly used biomedical balloon polymers. This approach ensured accurate interaction between the balloon and stent during the expansion phase.

The balloon was made of polyurethane and modelled as a hyper-elastic, non-compliant material to reflect its behavior during stent deployment. The hyper-elastic response was described using the Mooney-Rivlin strain energy function, defined mathematically as:

$$W = C_{10}(I_1 - 3) + C_{01}(I_2 - 3) + \frac{(J-1)^2}{D_1} \quad (1)$$

where $I_1$ and $I_2$ are the first and second stretch invariants, J is the volumetric stretch (third stretch invariant), and $C_{10}$, $C_{01}$, and $D_1$ are model parameters. The values of these parameters were determined experimentally and are provided in Table 2. Additionally, the polyurethane material had a density of 1070 kg/m$^3$, as specified for the simulation [37]. The artery was excluded from the model to focus on stent-specific mechanical responses, with boundary conditions validated to account for plaque and arterial interactions.

**Table 2: Mooney-Rivlin model parameters for balloon**

| Material | Density (Kg/mm$^3$) | $C_{10}$ | $C_{01}$ | $D_1$ |
|---|---|---|---|---|
| Polyurethane | 1070 | 1.03 | 3.69 | 0 |

### 2.3 Computational Framework and System Specifications

The cardiovascular stent architectures were developed using SolidWorks 2021 Professional Edition for parametric geometric modeling, ensuring precise dimensional control essential for biomedical applications. Comprehensive numerical investigations were performed within Abaqus CAE 6.14, employing static implicit solution algorithms to address the complex nonlinear mechanics inherent in stent deployment processes.

The computational infrastructure utilized a high-performance workstation featuring 16 GB DDR4 memory, Intel Core i7 13th generation processor (1.7 GHz base frequency), and 512 GB solid-state storage operating within Microsoft Windows 11 environment. This configuration provided optimal processing capabilities for large-scale finite element models and efficient post-processing operations.

### 2.4 Mesh Module

To ensure accurate representation of stent deformation and balloon interaction, the geometry was discretized using appropriate element types and mesh densities. The stent structure was meshed with **C3D10** (10-node quadratic tetrahedral elements), which are well-suited for capturing the complex geometry and large deformation behavior of stent struts. A **global seed size of 0.3 mm** was used for the stent to balance accuracy and computational cost.

The balloon was modeled using **S4R** elements (4-node doubly curved, reduced-integration shell elements with finite membrane strains), as these are widely adopted for thin-walled hyperelastic structures undergoing large strains. The balloon mesh employed a **global seed size of 0.4 mm**.

Mesh sensitivity was evaluated by observing displacement and stress results across different stent thicknesses ranging from 0.05 mm to 0.30 mm. The number of nodes and elements for each thickness configuration is summarized in **Table 3**. A representative meshed model showing the stent and balloon assembly is displayed in **Figure 3**.

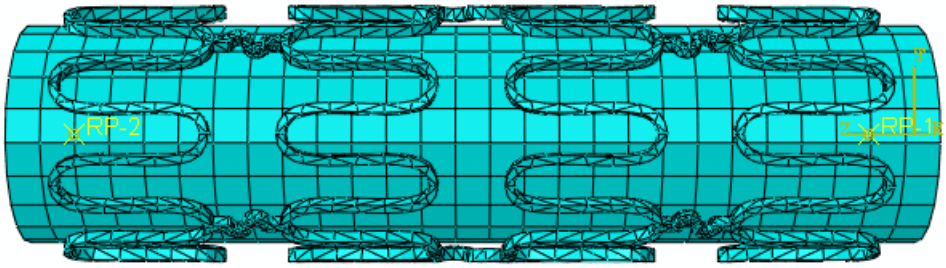


**Figure 3: Finite element mesh of the stent and balloon assembly.**

**Table 3: Mesh statistics for different stent thicknesses**

| Stent Thickness (mm) | Length (mm) | Inner Diameter (mm) | Strut Width (mm) | Elements | Nodes |
|---|---|---|---|---|---|
| 0.05 | 9.9 | 2.875 | 0.1 | 5954 | 15280 |
| 0.10 | 9.9 | 2.875 | 0.1 | 6597 | 16252 |
| 0.15 | 9.9 | 2.875 | 0.1 | 7048 | 16889 |

| | | | | | |
|---|---|---|---|---|---|
| 0.20 | 9.9 | 2.875 | 0.1 | 10263 | 23230 |
| 0.25 | 9.9 | 2.875 | 0.1 | 8869 | 20274 |
| 0.30 | 9.9 | 2.875 | 0.1 | 10077 | 20824 |

### 2.5 Stent Deployment: Boundary Conditions and Load Application

The simulation began with the stent in a crimped configuration, featuring an initial inner diameter of 3 mm. A cylindrical balloon was positioned concentrically within the stent to replicate the deployment mechanism. The applied boundary conditions are illustrated in Figure 4, which presents the top view of the stent and balloon assembly during the pre-expansion stage.

To emulate the physical constraints typically imposed by a catheter during stent deployment, the proximal end of the stent was constrained such that both axial displacement and rotational motion were restricted (i.e., Uz = 0, URz = 0). This setup prevented unwanted translational or torsional movement at the inlet. In contrast, the distal end remained free, allowing for natural shortening along the axial direction, thereby enabling accurate assessment of foreshortening during expansion. The interaction between the stent and the balloon surface was modeled using a surface-to-surface contact formulation, incorporating a friction coefficient of 0.1, which approximates the resistance typically encountered between polymeric balloons and metallic stent surfaces.

The inflation and deflation of the balloon were governed by a prescribed displacement boundary condition defined via a tabular amplitude curve (AMP-1) in Abaqus. This loading profile consisted of three sequential phases: balloon inflation, a brief holding period, and deflation. To ensure numerical stability and physical realism, the amplitude curve included gradual transitions between loading phases, with the default smoothing option enabled.

The total displacement applied to the balloon surface was set to $\Delta U_{max}$= 1.5 mm, corresponding to a 100% increase in the stent's diameter, effectively expanding it from 3 mm to approximately 6 mm. The loading sequence was distributed over a simulation time of 1 second. Specifically, at $t_1 = 0$ s, the displacement amplitude was set to zero (initial state); at $t_2 = 0.45$ s, it reached a maximum value of one (full inflation); at $t_3 = 0.55$ s, the amplitude dropped to 0.3 (holding phase); and at $t_4 = 1.0$ s, the amplitude returned to zero (complete deflation).

To reduce computational burden and streamline the simulation workflow, the effects of hemodynamic pressure were not considered, and the pre-folded balloon geometry was not modeled. These simplifications were intentionally adopted without compromising the study's focus on evaluating the stent's mechanical response during expansion. All simulations were conducted under identical loading and boundary conditions to ensure consistency across the various stent geometries analyzed.

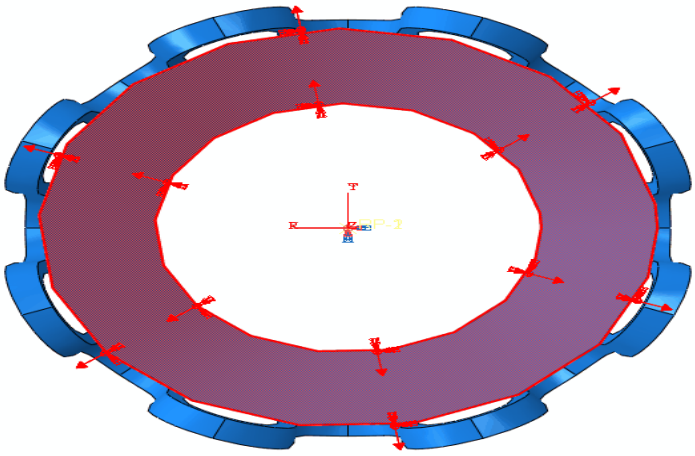

**Figure 4: Top view of stent and balloon assembly showing boundary conditions and initial setup used in the deployment simulation.**

### 2.6 Performance Evaluation of Stent Design

The functional effectiveness of a cardiovascular stent is significantly influenced by specific post-deployment behaviors. In this study, three key parameters **foreshortening**, **dogboning**, and **recoiling** were evaluated to assess the mechanical response of the stent design during and after expansion.

**Foreshortening** refers to the reduction in the stent's axial length following full deployment. This dimensional change can compromise the accuracy of stent placement within the target vessel. It is quantified as a percentage using the following relationship:

$$\text{Foreshortening } (\%) = \frac{L_0 - L_d}{L_0} \times 100 \tag{2}$$

where $L_0$ is the initial (crimped) length of the stent and $L_d$ is the final deployed length. A lower foreshortening value indicates better positional stability and predictability during implantation.

**Dogboning** describes the uneven radial expansion of the stent, typically observed when the proximal and distal ends expand more than the midsection. This phenomenon can lead to excessive stress concentrations at the arterial wall, increasing the risk of vessel injury. Dogboning is calculated using the equation:

$$\text{Dogboning } (\%) = \frac{D_{\text{max}} - D_{\text{mid}}}{D_{\text{mid}}} \times 100 \tag{3}$$

where $D_{\text{max}}$ is the maximum diameter observed at either end of the stent and $D_{\text{mid}}$ is the diameter at the midpoint.

**Recoiling** refers to the elastic recovery of the stent after balloon deflation, which may result in a slight reduction in diameter. This behavior is especially critical in maintaining luminal patency. Recoiling is determined as:

$$\text{Recoiling } (\%) = \frac{D_{\text{expanded}} - D_{\text{final}}}{D_{\text{expanded}}} \times 100 \tag{4}$$

where $D_{\text{expanded}}$ is the maximum diameter during peak balloon inflation, and $D_{\text{final}}$ is the stabilized diameter after deflation.

These mechanical indicators were measured at the **proximal end and distal end** of the stent structure to ensure consistent evaluation across all thickness variations. Proper analysis of these metrics is essential for optimizing the stent design and improving its clinical reliability.

## 3. Result

In this section a discussion of the achieved results is provided. The study is performed in two stages. During the first stage of the cardiovascular design, the material used is WE43 which was also used by another author in [38] The performance of both the design is compared. In the second stage of design optimization, the proposed design of the stent was kept same, but the material was changed. The first material was WE43, however, during the second stage, the material was changed to Zi-0.8Li-0.4Mg. The performance of both the design are compared in the second stage of the analysis.

### 3.1 Stent Deployment Analysis

This section provides a detailed analysis stent deployment as shown in figure 5. This figure shows the deformation behaviour of a cardiovascular stent with 0.5mm thickness during the deployment process. The simulation includes three stage: before balloon inflation, after balloon inflation, and after balloon deflation each visualised through Von Mises stress distribution.

**Before Balloon Inflation**

In the pre-inflation state, the stent remains in its crimped configuration, tightly compacted against the balloon. The structure is symmetric and uniformly arranged, with minimal internal stress, as indicated by the dominant deep blue coloration representing near-zero Von Mises stress values (0~100 KPa). This phase confirms that the stent is in an undeformed, stress-free state, crucial for safe navigation through the vasculature prior to deployment.

**After Balloon Inflation**

Upon inflation, the balloon expands radially, causing the stent to undergo significant plastic deformation. The stent struts expand outward, conforming to the balloon shape and increasing in diameter. The Von Mises stress distribution reveals elevated stress levels in the curved regions of the struts, with localized stress hotspots reaching above 1000 KPa, depicted in yellow to red zones. This indicates areas of maximum plastic deformation, which are expected in regions experiencing high bending and stretching. The uniformity of the deformation suggests that the stent design responds predictably and symmetrically to balloon expansion, which is essential for reliable vessel wall apposition.

**After Balloon Deflation**

Following balloon deflation, the stent remains partially deformed, having undergone elastic recoil. While the diameter decreases slightly, the stent retains most of its expanded shape, confirming that permanent plastic deformation has been achieved. The stress distribution is reduced compared to the inflation phase, now primarily in the green-to-blue range (below ~1000 KPa), indicating residual stresses present in the structure. These residual stresses are common and are a result of the material's elastic recovery. The stent configuration remains stable, and the ends show minimal inward collapse, supporting good radial strength and structural integrity.

**Before Balloon Inflation**

a

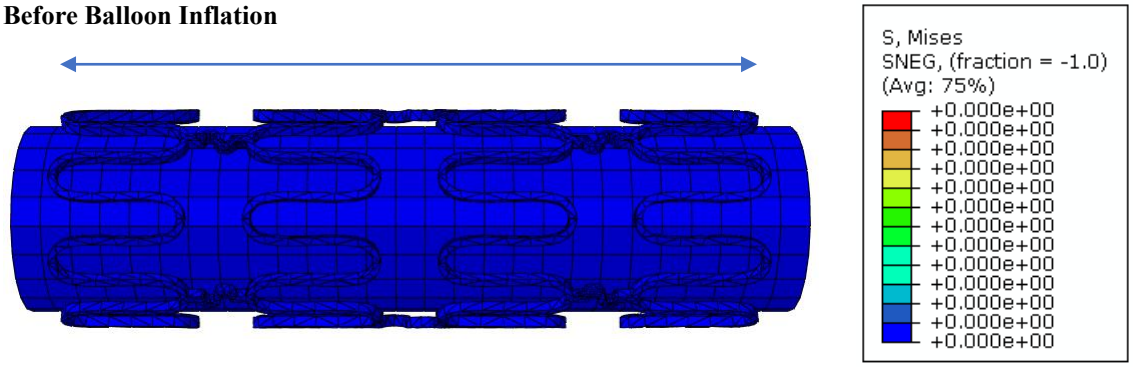


**After Balloon Inflation**

b

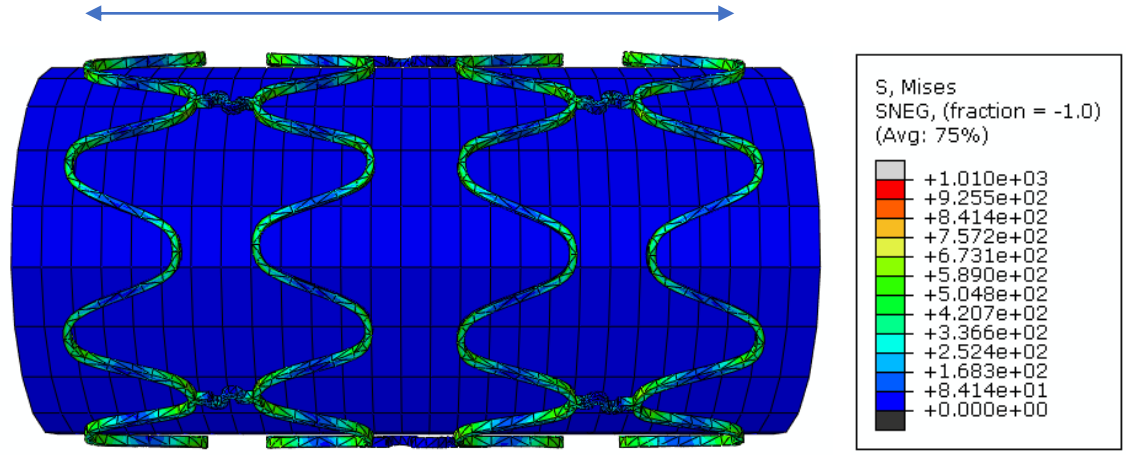

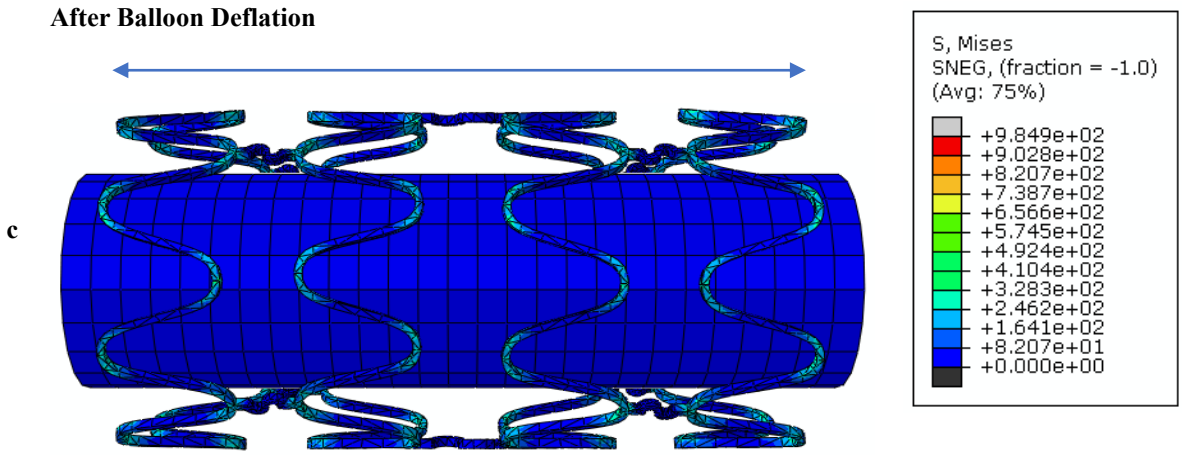


**Figure 5. Stent deployment phases and performance analysis. (a) Pre-inflation compressed geometry, (b) fully expanded configuration, (c) post-deflation performance metrics showing foreshortening, dogboning, and recoiling characteristics.**

### 3.2 Kinematics of Stent Length

Figure **6** illustrates the kinematics of stent length during the expansion process for a stent with a wall thickness of 0.15 mm. The stent length, denoted as L, is plotted as a function of time over the course of the expansion, providing direct insight into axial deformation behavior, commonly referred to as foreshortening.

The stent initially maintains a stable length of approximately 9.9 mm at time t=0 seconds, indicating an undeformed state prior to the onset of balloon inflation. As time progresses, the stent begins to expand radially, and a simultaneous axial contraction is observed, resulting in a progressive reduction in length.

Between 0.05 and 0.45 seconds, a steep and continuous decline in stent length occurs, reaching a minimum value of approximately 9.524 mm, corresponding to a maximum foreshortening effect. This segment represents the active expansion phase, during which the stent undergoes plastic deformation and adjusts to the internal pressure exerted by the balloon. The maximum change in length is approximately 3.8%. This value is notably lower than those reported in traditional stent designs, indicating an excellent axial deployment profile.

Following this contraction phase, a plateau is observed between 0.45 and 0.65 seconds, during which the stent length stabilizes at its minimum. This plateau suggests a saturation point where axial deformation ceases, and radial expansion becomes dominant. Post 0.65 seconds, a partial recovery in length is detected, with the final stent length stabilizing around 9.615 mm. This small rebound may be attributed to elastic relaxation or mechanical adjustment as the balloon pressure is released and the stent settles into the vessel wall. However, this recovery does not significantly compromise the reduced foreshortening achieved during expansion. The foreshortening after the balloon pressure is released is 0.95%.

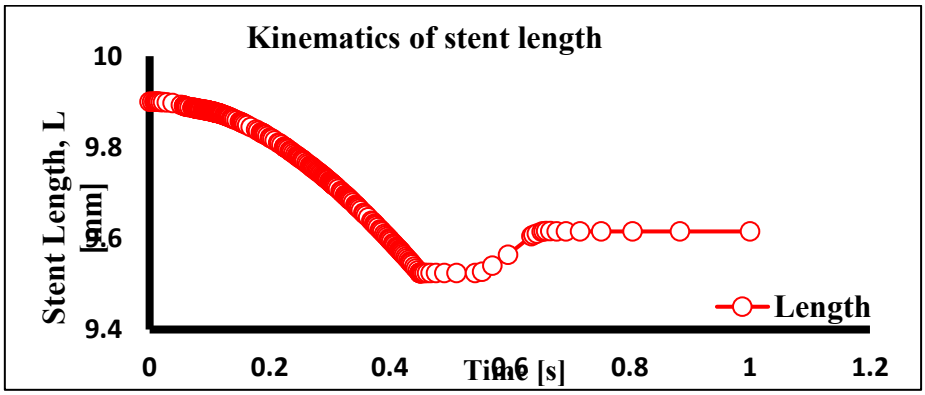


**Figure 6. shows the Kinematics of stent length for Material Zn-0.8Li-.04Mg with thickness of 0.15 mm**

Figure **7** presents the temporal evolution of stent diameter during balloon expansion for a stent with a wall thickness of 0.15 mm. The graph displays the change in diameter D as a function of time, offering insight into the radial expansion dynamics, which directly complement axial behaviour (length shortening) in analysing foreshortening characteristics.

At t=0 seconds, the stent begins with an initial crimped diameter of approximately 2.875 mm, which is characteristic of a pre-deployed configuration designed to navigate through the vasculature. From 0 to ~0.45 seconds, the stent undergoes progressive radial expansion, with diameter increasing sharply and linearly up to 5.83 mm. This phase represents the balloon inflation and stent expansion stage, during which the radial stress exceeds the yield strength of the Zn-0.8Li-0.4Mg alloy, leading to plastic deformation and outward expansion. Between 0.45 and 0.55 seconds, the diameter curve reaches a maximum and begins to slightly decrease, eventually stabilizing around 5.374 mm. This modest decline suggests the occurrence of elastic recoil, where the stent partially contracts after balloon deflation due to internal restoring forces.

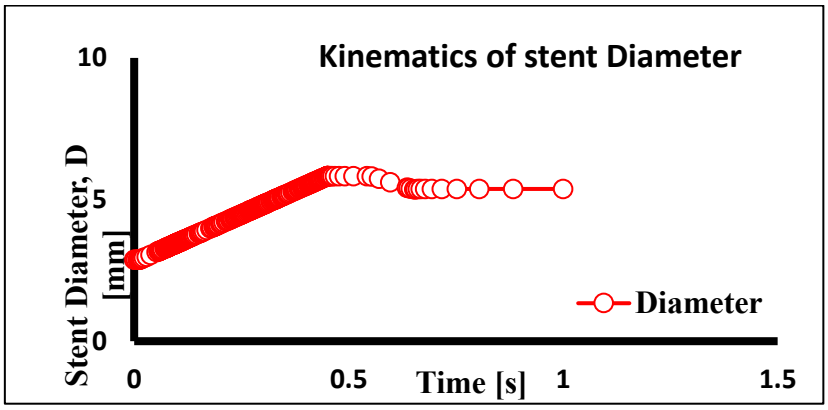


**Figure 7. shows the Kinematics of stent diameter for Material Zn-0.8Li-.04Mg with thickness of 0.15 mm**

### 3.3 Proposed Design with WE43 stent material

To evaluate the mechanical performance of the newly designed cardiovascular stent using WE43 magnesium alloy, three critical parameters were assessed foreshortening, dogboning, and recoilingacross a range of stent thicknesses (0.05–0.30 mm). These parameters are fundamental indicators of stent deployment accuracy, uniformity of expansion, and post-expansion stability. For performance evaluation, the results were compared with an existing dataset from earlier research that employed the same material.

**Foreshortening**

Foreshortening represents the axial shortening of a stent during deployment. Minimizing this parameter is crucial to ensure accurate lesion coverage and optimal vascular scaffolding. As shown in Table 4, the current design demonstrates a pronounced reduction in foreshortening across all thicknesses when compared to the published result. Specifically, at a 0.05 mm thickness, foreshortening decreased from 5.74% to 0.79%, while the average reduction across all thicknesses is approximately 83%.

**Table 4: Foreshortening Comparison Between Published Results [38] and Present Study**

| Stent Thickness (mm) | Reference Study (%) | Present Study (%) |
|---|---|---|
| 0.05 | 5.74 | 0.79 |
| 0.10 | 5.72 | 0.82 |
| 0.15 | 5.43 | 0.97 |
| 0.20 | 5.57 | 1.15 |
| 0.25 | 5.625 | 0.89 |

| | | |
|---|---|---|
| 0.30 | 5.50 | 1.20 |

This substantial improvement suggests superior structural design and expansion behaviour, likely attributable to optimized strut geometry and enhanced uniformity in plastic deformation. From a clinical perspective, the minimized foreshortening ensures more predictable stent length during deployment, thereby reducing the likelihood of incomplete lesion coverage or stent misplacement.

**Dogboning**

Dogboning, which reflects uneven radial expansion where the stent ends inflate more than the midsection, was evaluated across varying thicknesses. As shown in Table 5, the reference study recorded negative dogboning values for lower thicknesses (0.05–0.15 mm), indicating under-expansion at the stent ends. In contrast, the present design showed consistently positive and controlled dogboning values, demonstrating more uniform expansion.

**Table 5: Comparison of Dogboning Between Reference Study [38] and Present Design**

| Stent Thickness (mm) | Reference Study (%) | Present study (%) |
|---|---|---|
| 0.05 | -0.038 | 1.65 |
| 0.10 | -0.060 | 0.82 |
| 0.15 | -0.018 | 0.72 |
| 0.20 | 0.008 | 0.78 |
| 0.25 | 0.030 | 0.83 |
| 0.30 | 0.068 | 0.80 |

The lowest dogboning in the present design was observed at 0.15 mm thickness, with a value of 0.72%, indicating near-symmetric radial deployment. Overall, all values in the current design remained below 1.65%, suggesting improved mechanical behavior and reduced stress variation along the stent length. These findings confirm that the proposed geometry enhances expansion uniformity across all thicknesses evaluated.

**Recoiling**

Recoiling, defined as the elastic contraction of the stent post-deployment, directly impacts lumen stability and long-term patency. Lower recoil values are indicative of higher radial strength and better structural performance. As presented in Table 6, the proposed stent design exhibited a higher recoil at the minimum thickness of 0.05 mm (9.16%) compared to the reference value (3.80%), suggesting inadequate resistance due to reduced structural rigidity.

**Table 6: Recoil Comparison Between Reference Study [38] and Present Design**

| Stent Thickness (mm) | Reference Study (%) | Present study (%) |
|---|---|---|
| 0.05 | 3.80 | 9.16 |
| 0.10 | 8.20 | 8.49 |
| 0.15 | 11.70 | **8.03** |
| 0.20 | 14.40 | 8.09 |
| 0.25 | 15.80 | 8.31 |
| 0.30 | 17.10 | 8.03 |

However, for all other thicknesses (0.10 mm and above), the current design demonstrated a consistent reduction in recoil compared to the reference. The average recoil across these thicknesses in the present study was 8.18%, significantly lower than the 11.52% reported in the earlier work—yielding an improvement of approximately 29%.

The most stable performance was observed at 0.15 mm and 0.30 mm, both showing the lowest recoil of 8.03%, indicating an optimal balance between structural stiffness and flexibility. This trend highlights the effectiveness of the improved geometry in enhancing radial strength, particularly critical for bioresorbable stents, where early mechanical support is essential before the onset of degradation.

**Overall Performance Evaluation**

The current stent design demonstrates marked improvements over the reference across all three mechanical parameters. The most significant gain is observed in foreshortening, with values reduced by approximately 83%, improving axial stability. Recoiling is also significantly minimized, showing a 29% decrease, enhancing radial strength. While dogboning in the present design remains slightly positive, it stays well within safe and clinically acceptable limits, reflecting uniform radial expansion. These enhancements are particularly prominent in mid-to-high thickness ranges (0.15–0.30 mm).

**Table 7: Comparison of the design performance**

| Parameter | Reference Avg | Present Study Avg | Improvement |
|---|---|---|---|
| Foreshortening (%) | 5.60 | 0.97 | ~83% reduction |
| Dogboning (%) | ~0.00 | 0.93 | Controlled, within safe limits |
| Recoiling (%) | 11.52 | 8.18 | ~29% reduction |

A combined evaluation of foreshortening, dogboning, and recoiling across six stent thicknesses reveals that **0.15 mm** offers the most balanced performance. It records the **lowest dogboning (0.72%)** and **lowest recoiling (8.03%)**, while maintaining minimal foreshortening (**0.97%**), indicating excellent axial and radial stability. Although **0.30 mm** also shows low recoil (**8.03%**) and moderate dogboning (**0.80%**), its foreshortening is relatively higher (**1.20%**). Therefore, **0.15 mm** is identified as the **optimal thickness**, offering superior mechanical behavior suitable for bioresorbable stent applications.

The graphical representation of each parameter is presented in figure 8.

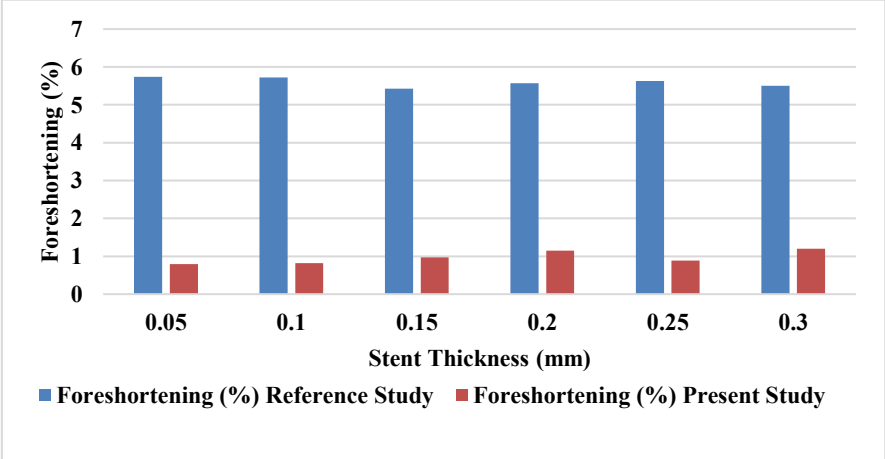


**(a)**

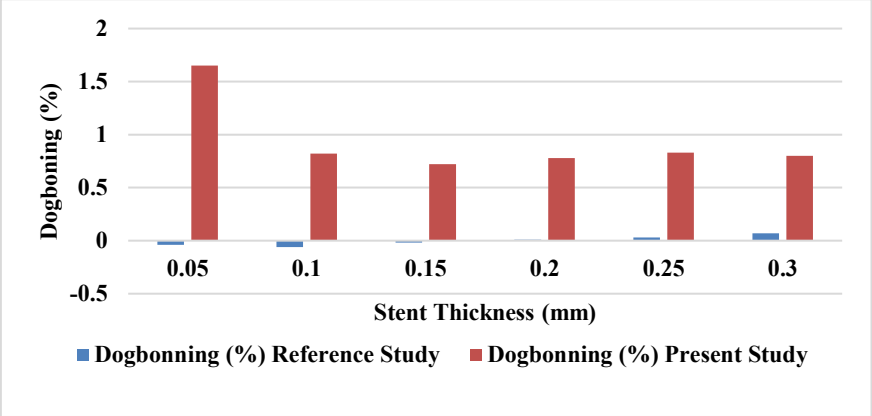


**(b)**

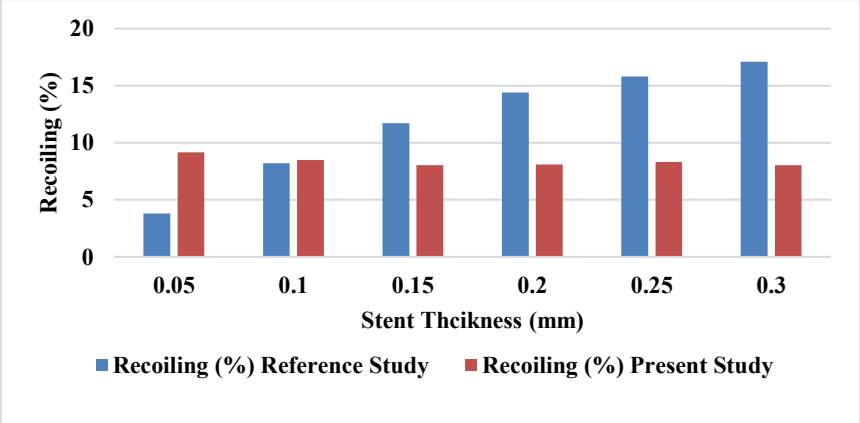


**(c)**

**Figure 8: Graphical Comparison of (a) Foreshortening, (b) Dogboning, and (c) Recoiling**

**Clinical and Engineering Implications**

The enhanced mechanical performance of the proposed stent design, particularly in reducing foreshortening and recoil, has direct implications for improving patient outcomes. Precise stent placement, coupled with long-term luminal stability, reduces the risks of restenosis, edge dissection, and incomplete lesion coverage. Furthermore, the controlled dogboning ensures a more even stress distribution along the arterial wall, promoting better vascular healing. From a manufacturing perspective, these results underscore the potential of advanced finite element optimization and material tailoring in developing next-generation bioresorbable stents using WE43 alloy.

### 3.4 Material Comparative Study (Zn–0.8Li–0.4Mg vs WE43)

The second phase of the study aimed to assess the influence of stent material selection on deployment behaviour and mechanical performance. For this, the optimized stent geometry was retained while substituting the WE43 alloy with a Zn–0.8Li–0.4Mg alloy. This zinc-based biodegradable alloy is known for its biocompatibility and intermediate degradation kinetics, offering a potential alternative to magnesium-based systems.

**Foreshortening**

Foreshortening reflects axial contraction during expansion and directly affects precision in lesion coverage. As shown in Table 8, both materials demonstrate comparable behavior. Zn–0.8Li–0.4Mg recorded slightly higher or equivalent foreshortening at lower thicknesses (e.g., 0.05 mm: 0.8% vs 0.79%), but the overall trend shows the values remain within a ±0.05% deviation from those observed with WE43.

**Table 8: Foreshortening Comparison for WE43 vs Zn-0.8Li-0.4Mg**

| Stent Thickness (mm) | WE43 (%) | Zn–0.8Li–0.4Mg (%) |
|---|---|---|
| 0.05 | 0.79 | 0.80 |
| 0.10 | 0.82 | 0.81 |
| 0.15 | 0.97 | 0.95 |
| 0.20 | 1.15 | 1.12 |
| 0.25 | 0.89 | 0.87 |
| 0.30 | 1.20 | 1.08 |

The Zn–0.8Li–0.4Mg alloy achieves equally low foreshortening across all thicknesses. Notably, at higher thicknesses (≥0.25 mm), the foreshortening is marginally reduced in comparison to WE43 as shown in table 8. These findings suggest that the Zn-based alloy offers comparable or slightly improved axial deployment stability, preserving stent length more consistently.

**Dogboning**

Uniform radial expansion is critical to minimizing vascular trauma. The dogboning results indicate a similar trend between both materials, with Zn–0.8Li–0.4Mg demonstrating slightly reduced values across most thicknesses.

**Table 9: Dogboning Comparison for WE43 vs Zn-0.8Li-0.4Mg**

| Stent Thickness (mm) | WE43 (%) | Zn–0.8Li–0.4Mg (%) |
|---|---|---|
| 0.05 | 1.65 | 1.48 |
| 0.10 | 0.82 | 0.82 |
| 0.15 | 0.72 | 0.74 |
| 0.20 | 0.78 | 0.77 |
| 0.25 | 0.83 | 0.82 |
| 0.30 | 0.80 | 0.85 |

For thinner stents (0.05 mm), Zn–0.8Li–0.4Mg exhibits lower dogboning (1.48% vs 1.65%), indicating more uniform end-to-center expansion. Across the mid-thickness range, differences are negligible. This outcome indicates that Zn–0.8Li–0.4Mg maintains a consistent expansion profile and may offer improved radial symmetry at ultra-thin profiles.

**Recoiling**

The most marked difference between the two materials is seen in recoil resistance, a crucial parameter determining post-deployment lumen stability as shown in table 10.

**Table 10: Recoiling Comparison for WE43 vs Zn-0.8Li-0.4Mg**

| Stent Thickness (mm) | WE43 | Zn–0.8Li–0.4Mg |
|---|---|---|
| 0.05 | 9.16 | 8.78 |
| 0.10 | 8.49 | 8.28 |
| 0.15 | 8.03 | 7.82 |
| 0.20 | 8.09 | 7.87 |

| | | |
|---|---|---|
| 0.25 | 8.31 | 8.11 |
| 0.30 | 8.03 | 7.90 |

The Zn–0.8Li–0.4Mg alloy consistently demonstrates lower recoil values across all thicknesses, with an average reduction of ~2.5%. For instance, at 0.05 mm thickness, recoil drops from 9.16% to 8.78%, and at 0.20 mm from 8.09% to 7.87%. This improved behaviour suggests a material with enhanced elastic stability, likely due to a more favourable modulus-to-yield ratio.

### 3.3 Overall Material Performance Assessment

**Table 11: Overall material performance**

| Metric | WE43 (Avg) | Zn–0.8Li–0.4Mg (Avg) | Observations |
|---|---|---|---|
| Foreshortening (%) | 0.97 | 0.92 | Comparable, with slight improvement at 0.3 mm |
| Dogboning (%) | 0.93 | 0.91 | Nearly identical performance |
| Recoiling (%) | 8.52 | 8.29 | Zn alloy consistently outperforms WE43 |

The substitution of WE43 with Zn–0.8Li–0.4Mg in the same stent design results in comparable or improved mechanical behaviour across key performance metrics. Most notably:

- Recoiling is reduced across all configurations, enhancing post-expansion diameter retention.
- Foreshortening remains within optimal limits, with marginal improvement at higher thicknesses.
- Dogboning values remain controlled, ensuring radial uniformity.

From a clinical and engineering standpoint, Zn–0.8Li–0.4Mg emerges as a viable alternative to WE43, particularly for stents where controlled degradation and elastic stability are critical. Its performance across all metrics indicates potential for longer-term luminal support with minimal structural compromise, making it a strong candidate for next-generation bioresorbable cardiovascular scaffolds.

## Conclusion

This study presents a comprehensive evaluation of a novel cardiovascular stent design utilizing the biodegradable alloy WE43, with particular focus on deployment mechanics, material response, and performance across varying thicknesses. The results demonstrate a substantial reduction in foreshortening from 5.74% in the base study to as low as 0.79% thereby significantly enhancing lesion coverage accuracy. Dogbonning was consistently maintained within clinically acceptable limits across all thicknesses, while recoiling was markedly reduced at higher thickness values (from 17.1% to 8.03%), affirming improved radial strength and structural resilience post-deployment. Comparative analysis with Zn–0.8Li–0.4Mg further validated the superior mechanical behavior of WE43 in terms of controlled expansion, minimal post-inflation deformation, and stable final configuration. Kinematic simulations of stent length and diameter, along with stress distribution analyses before, during, and after balloon inflation, confirmed the design's capacity to achieve predictable expansion with controlled stress localization and minimal elastic recoil. Overall, the findings substantiate the proposed stent geometry and material combination as a promising candidate for next-generation biodegradable vascular implants, offering enhanced deployment precision, mechanical reliability, and clinical safety.

## References

1. *World Health Organization. Cardiovascular Diseases (CVDs).*; 2021
2. Alam, A.; Rahyab, A.S.; Hughes, G.J. Percutaneous Coronary Intervention. In *A Medication Guide to Internal Medicine Tests and Procedures*; Elsevier, 2022; pp. 209–212 ISBN 978-0-323-79007-9.

3. Martin, H.; Grabow, N.; Stiehm, M.; Lootz, D.; Schmitz, K.P. Finite Element Analysis of Compliance of Stent-Vesselsystems. *Biomedical Engineering / Biomedizinische Technik* **2013**, doi:10.1515/bmt-2013-4111.

4. Wiyono, A.V.; Ardinal, A.P. Revolutionizing Cardiovascular Frontiers: A Dive Into Cutting-Edge Innovations in Coronary Stent Technology. *Cardiology in Review* **2024**, doi:10.1097/CRD.0000000000000705.

5. O'Brien, B.; Carroll, W. The Evolution of Cardiovascular Stent Materials and Surfaces in Response to Clinical Drivers: A Review. *Acta Biomaterialia* **2009**, *5*, 945–958, doi:10.1016/j.actbio.2008.11.012.

6. Tibayan, Y.; Cigarroa, J. In Stent Restenosis Remains a Clinically Relevant Problem. *Cathet Cardio Intervent* **2013**, *81*, 266–267, doi:10.1002/ccd.24790.

7. O'Brien, B.J.; Stinson, J.S.; Larsen, S.R.; Eppihimer, M.J.; Carroll, W.M. A Platinum–Chromium Steel for Cardiovascular Stents. *Biomaterials* **2010**, *31*, 3755–3761, doi:10.1016/j.biomaterials.2010.01.146.

8. Khan, W.; Thipparaboina, R.; Farah, S.; Weinberger, J.Z.; Domb, A.J. Drug-Eluting Stents. In *Focal Controlled Drug Delivery*; Domb, A.J., Khan, W., Eds.; Advances in Delivery Science and Technology; Springer US: Boston, MA, 2014; pp. 387–403 ISBN 978-1-4614-9433-1.

9. Maulik Patel Drug Eluting Stent for Restenosis Diseases. *Afr. J. Pharm. Pharmacol.* **2012**, *6*, doi:10.5897/AJPP11.107.

10. McFadden, E.P.; Stabile, E.; Regar, E.; Cheneau, E.; Ong, A.T.; Kinnaird, T.; Suddath, W.O.; Weissman, N.J.; Torguson, R.; Kent, K.M.; et al. Late Thrombosis in Drug-Eluting Coronary Stents after Discontinuation of Antiplatelet Therapy. *The Lancet* **2004**, *364*, 1519–1521, doi:10.1016/S0140-6736(04)17275-9.

11. Brener, S.J. Are at Least 12 Months of Dual Antiplatelet Therapy Needed for All Patients With Drug-Eluting Stents?: All Patients With Drug-Eluting Stents Need at Least 12 Months of Dual Antiplatelet Therapy. *Circulation* **2015**, *131*, 2001–2009, doi:10.1161/CIRCULATIONAHA.114.013279.

12. Iqbal, J.; Onuma, Y.; Ormiston, J.; Abizaid, A.; Waksman, R.; Serruys, P. Bioresorbable Scaffolds: Rationale, Current Status, Challenges, and Future. *European Heart Journal* **2014**, *35*, 765–776, doi:10.1093/eurheartj/eht542.

13. Lammer, J. Commentary: Bioresorbable Drug-Eluting Scaffold for Peripheral Artery Disease: The Best of Two Worlds or Unnecessary? *J Endovasc Ther* **2020**, *27*, 623–625, doi:10.1177/1526602820928591.

14. Gąsior, P.; Cheng, Y.; Ferrone, M.; McGregor, J.; Conditt, G.; Granada, J.; Kaluza, G.L. Early Scaffold Strut Coverage in Ultra-High Molecular Weight Amorphous PLLA Sirolimus-Eluting Bioresorbable Scaffolds: Impact of Strut Thickness Assessed in Normal Porcine Coronary Arteries. *pwki* **2020**, *16*, 102–106, doi:10.5114/aic.2020.93917.

15. Barkholt, T.Ø.; Webber, B.; Holm, N.R.; Ormiston, J.A. Mechanical Properties of the Drug-eluting Bioresorbable Magnesium Scaffold Compared with Polymeric Scaffolds and a Permanent Metallic Drug-eluting Stent. *Cathet Cardio Intervent* **2020**, *96*, doi:10.1002/ccd.28545.

16. Gao, J.-C.; Hu, D.; Song, C.-J. Medical Magnesium Alloy Degradation and Its Impact on Human Physiology. *Gongneng Cailiao/Journal of Functional Materials* **2012**, *43*, 2577–2583.

17. Peuster, M.; Hesse, C.; Schloo, T.; Fink, C.; Beerbaum, P.; Von Schnakenburg, C. Long-Term Biocompatibility of a Corrodible Peripheral Iron Stent in the Porcine Descending Aorta. *Biomaterials* **2006**, *27*, 4955–4962, doi:10.1016/j.biomaterials.2006.05.029.

18. Bowen, P.K.; Drelich, J.; Goldman, J. Zinc Exhibits Ideal Physiological Corrosion Behavior for Bioabsorbable Stents. *Advanced Materials* **2013**, *25*, 2577–2582, doi:10.1002/adma.201300226.

19. Mostaed, E.; Sikora-Jasinska, M.; Mostaed, A.; Loffredo, S.; Demir, A.G.; Previtali, B.; Mantovani, D.; Beanland, R.; Vedani, M. Novel Zn-Based Alloys for Biodegradable Stent Applications: Design, Development and in Vitro Degradation. *Journal of the Mechanical Behavior of Biomedical Materials* **2016**, *60*, 581–602, doi:10.1016/j.jmbbm.2016.03.018.

20. Vojtěch, D.; Kubásek, J.; Šerák, J.; Novák, P. Mechanical and Corrosion Properties of Newly Developed Biodegradable Zn-Based Alloys for Bone Fixation. *Acta Biomaterialia* **2011**, *7*, 3515–3522, doi:10.1016/j.actbio.2011.05.008.

21. Shi, Z.-Z.; Gao, X.-X.; Zhang, H.-J.; Liu, X.-F.; Li, H.-Y.; Zhou, C.; Yin, Y.-X.; Wang, L.-N. Design Biodegradable Zn Alloys: Second Phases and Their Significant Influences on Alloy Properties. *Bioactive Materials* **2020**, *5*, 210–218, doi:10.1016/j.bioactmat.2020.02.010.

22. Liu, A.; Lu, Y.; Dai, J.; Wen, P.; Xia, D.; Zheng, Y. Mechanical Properties, in Vitro Biodegradable Behavior, Biocompatibility and Osteogenic Ability of Additively Manufactured Zn-0.8Li-0.1Mg Alloy Scaffolds. *Biomaterials Advances* **2023**, *153*, 213571, doi:10.1016/j.bioadv.2023.213571.

23. Yang, H.; Wang, C.; Liu, C.; Chen, H.; Wu, Y.; Han, J.; Jia, Z.; Lin, W.; Zhang, D.; Li, W.; et al. Evolution of the Degradation Mechanism of Pure Zinc Stent in the One-Year Study of Rabbit Abdominal Aorta Model. *Biomaterials* **2017**, *145*, 92–105, doi:10.1016/j.biomaterials.2017.08.022.

24. Moravej, M.; Mantovani, D. Biodegradable Metals for Cardiovascular Stent Application: Interests and New Opportunities. *IJMS* **2011**, *12*, 4250–4270, doi:10.3390/ijms12074250.

25. Pant, S.; Bressloff, N.W.; Limbert, G. Geometry Parameterization and Multidisciplinary Constrained Optimization of Coronary Stents. *Biomech Model Mechanobiol* **2012**, *11*, 61–82, doi:10.1007/s10237-011-0293-3.

26. Timmins, L.H.; Meyer, C.A.; Moreno, M.R.; Moore, J.E. Mechanical Modeling of Stents Deployed in Tapered Arteries. *Ann Biomed Eng* **2008**, *36*, 2042–2050, doi:10.1007/s10439-008-9582-0.

27. Colombo, A.; Stankovic, G.; Moses, J.W. Selection of Coronary Stents. *Journal of the American College of Cardiology* **2002**, *40*, 1021–1033, doi:10.1016/S0735-1097(02)02123-X.

28. Computational Design of Artificial Organs Available online: https://scispace.com/papers/computational-design-of-artificial-organs-3hjj2r19ye (accessed on 20 June 2025).

29. Lupi, A.; Schaffer, A.; Bongo, A.S. Should Ultrathin Strut Drug Eluting Stents Be Considered the New Benchmark for Novel Coronary Stents Approval? The Complex Interplay between Stent Strut Thickness, Polymeric Carriers and Antiproliferative Drugs. *J. Thorac. Dis.* **2018**, *10*, 678–681, doi:10.21037/jtd.2018.01.108.

30. Leone, A.; Simonetti, F.; Avvedimento, M.; Angellotti, D.; Immobile Molaro, M.; Franzone, A.; Esposito, G.; Piccolo, R. Ultrathin Struts Drug-Eluting Stents: A State-of-the-Art Review. *JPM* **2022**, *12*, 1378, doi:10.3390/jpm12091378.

31. Jiménez, J.M.; Davies, P.F. Hemodynamically Driven Stent Strut Design. *Ann Biomed Eng* **2009**, *37*, 1483–1494, doi:10.1007/s10439-009-9719-9.

32. Gijsen, F.J.; Migliavacca, F.; Schievano, S.; Socci, L.; Petrini, L.; Thury, A.; Wentzel, J.J.; Van Der Steen, A.F.; Serruys, P.W.; Dubini, G. Simulation of Stent Deployment in a Realistic Human Coronary Artery. *BioMed Eng OnLine* **2008**, *7*, 23, doi:10.1186/1475-925X-7-23.

33. Liu, S.; Yuan, C.; Gao, K.; Shi, R.; Zhu, B.; Pang, X. Degradation Characteristics and Biocompatibility of Zinc Alloy in Advanced Biomedical Bone Implants. *Langmuir* **2025**, *41*, 8711–8725, doi:10.1021/acs.langmuir.4c05260.

34. Liu, A.; Qin, Y.; Dai, J.; Song, F.; Tian, Y.; Zheng, Y.; Wen, P. Fabrication and Performance of Zinc-Based Biodegradable Metals: From Conventional Processes to Laser Powder Bed Fusion. *Bioactive Materials* **2024**, *41*, 312–335, doi:10.1016/j.bioactmat.2024.07.022.

35. Magnesium WE43-T6 Alloy (UNS M16600) Available online: https://www.azom.com/article.aspx?ArticleID=8539 (accessed on 21 June 2025).

36. Yang, H.; Jia, B.; Zhang, Z.; Qu, X.; Li, G.; Lin, W.; Zhu, D.; Dai, K.; Zheng, Y. Alloying Design of Biodegradable Zinc as Promising Bone Implants for Load-Bearing Applications. *Nat Commun* **2020**, *11*, 401, doi:10.1038/s41467-019-14153-7.

37. Karimi, A.; Navidbakhsh, M.; Yamada, H.; Razaghi, R. A Nonlinear Finite Element Simulation of Balloon Expandable Stent for Assessment of Plaque Vulnerability inside a Stenotic Artery. *Med Biol Eng Comput* **2014**, *52*, 589–599, doi:10.1007/s11517-014-1163-9.

38. Pang, T.Y.; Kwok, J.S.; Nguyen, C.T.; Fox, K. Evaluating Magnesium Alloy WE43 for Bioresorbable Coronary Stent Applications. *MRS Advances* **2021**, *6*, 54–60, doi:10.1557/s43580-021-00012-5.